

Formation of soot particles in Ar/H₂/CH₄ microwave discharges during nanocrystalline diamond deposition: A modeling approach*

K. Hassouni[‡], F. Mohasseb, F. Bénédic, G. Lombardi, and A. Gicquel

*LIMHP, CNRS-UPR1311, Université Paris 13, 99 Avenue J. B. Clément,
93430 Villetaneuse, France*

Abstract: Homogenous mechanism of soot formation in moderate-pressure Ar/CH₄/H₂ microwave discharges was analyzed with the help of kinetics modeling of the thermally non-equilibrium plasmas. Two main reaction mechanisms based on either neutral molecular growth and condensation reaction nucleation process were considered. These mechanisms were incorporated in a numerical model that solves for the plasma species and energy equations under a quasi-uniform plasma assumption. This enabled us to estimate the plasma species density and temperature along with the nucleation rate at different discharge conditions. The results showed that soot particles might form at significant density values by both neutral and ionic mechanisms. Their formation mainly takes place at the discharge edges where the temperature level favors the development of large molecular edifices. Simulations showed that the formation of soot is unlikely to happen in the bulk of the discharge where the gas temperature is high and the large molecular hydrocarbon (HC) cannot form at significant concentrations.

Keywords: plasma; kinetics; modeling; particles; hydrocarbon.

INTRODUCTION

Polycrystalline diamond (PCD) films were successfully deposited using plasma-enhanced chemical vapor deposition (PECVD) process at the end of the 1980s [1]. Since then, an extremely large number of studies were carried out to improve and optimize the deposition process for several applications in numerous fields such as optics, electronics, and mechanics. Despite this large effort, the industrial development of CVD diamond coating remains quite limited due to the difficulty encountered when trying to fit a well-designed laboratory process or material to the industrial needs. This is especially the case when the deposition process concerns complex shape materials and when difficult post-processing operations are required to make the coating suitable for the targeted application.

This last situation is particularly of concern in many applications where very low roughness coatings are required. A very long and complex polishing post-process is indeed required in this case. Recently, Gruen et al. proposed a new method to deposit nanocrystalline diamond (NCD) films with a roughness in the nanometer range [2]. The polishing post-process is no more required for this kind of film, which makes them much more convenient than PCD films for several applications. This is especially true for the development of surface acoustic wave (SAW) devices where the nanometer-scale

*Paper presented at the 17th International Symposium on Plasma Chemistry (ISPC 17), Toronto, Ontario, Canada, 7–12 August 2005. Other presentations are published in this issue, pp. 1093–1298.

[‡]Corresponding author: hassouni@limhp.univ-paris13.fr

roughness of NCD associated to its high characteristic elastic wave velocity makes it a very interesting material for the fabrication of high-frequency SAW devices [3].

The NCD deposition process as proposed by Gruen et al. makes use of Ar/CH₄ with low methane concentration, typically around 1 %. Bénédic et al. [4] investigated the use of such a mixture for the deposition of NCD in a plasma device that has proven to be very efficient for the deposition of high-purity PCD [5] as well as homoepitaxial monocrystalline diamond (MCD) [6]. Ar/CH₄ discharges turned out to be systematically very unstable in the microwave cavity coupling system used in this device. A small amount of hydrogen was therefore added in the feed gas, and the experiment carried out with a feed gas composition of 1 % methane, 2–7 % hydrogen, and 92–97 % argon allowed us to improve the discharge stability, and NCD deposition was achieved in some cases [4]. However, despite this improvement, Ar/H₂/CH₄ microwave discharges showed in some cases some long time-scale (i.e., several hours) instability, which yields a significant drift of the deposition process often associated with the production of soot particles in the plasma reactor. Therefore, it appears that the development of a very stable and reproducible process requires avoiding the soot formation. To reach this goal, it is necessary to understand the mechanism that leads to the soot production under the discharge conditions that are in principle suitable for NCD deposition. The objective of this paper is directly related to this last point.

Soot particles may form through either homogenous or heterogeneous mechanism. The later is not considered in this paper. The homogeneous nucleation is described using the “largest molecular edifice” concept, which assumes that the nucleation is the result of the development of large molecular structures up to a given size for which the molecular edifices undergo condensation process with a phase transition that leads to the formation of a solid nucleus [7]. The investigation of the solid particles formation requires, therefore, describing the detailed kinetics of the plasma. It is also necessary to model the formation of large molecules and their development. The evolution of the nuclei formed in the gas phase has, in principle, to be tracked by an aerosol dynamics model. However, this last point will not be addressed in the present paper, where we will mainly focus on the chemical kinetics, the molecular growth, and the nucleation rates.

MAIN CHARACTERISTICS OF THE INVESTIGATED PLASMAS

The plasma system used for the deposition of NCD films is depicted in Fig. 1 [8]. It consists of a microwave cavity coupling system where a microwave is generated by a magnetron device, propagated in a wave-guide and transferred in the cavity shown in Fig. 1. In this cavity, a standing wave system may form and a plasma may be ignited inside the low-pressure quartz bell jar. Optimal discharge conditions lead to the formation of a hemispherical plasma located just above the substrate surface on which diamond is deposited. This device is routinely used for the deposition of PCD and MCD when using a low methane content H₂/CH₄ feed gas [5,6]. The discharges in these conditions have been extensively investigated and characterized.

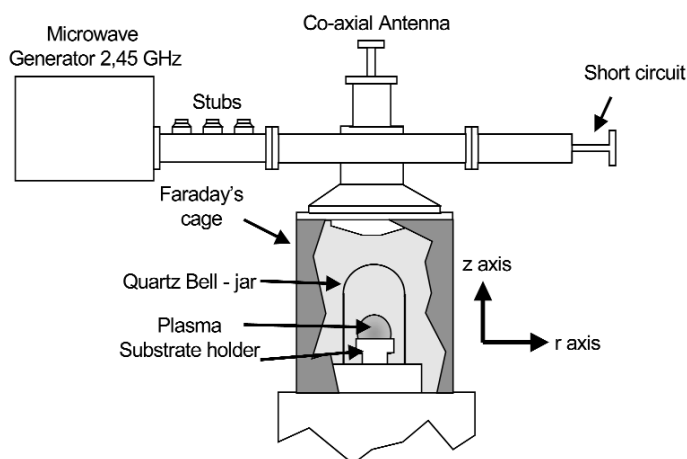


Fig. 1 Schematic of the microwave discharge system investigated in this work.

The discharges considered in this work for the deposition of NCD films are fairly different. They make use of feed gas mixtures containing CH_4 , hydrogen and argon with typical concentrations of 1, 2–7, and 92–97 %, respectively. For a given input microwave power, these discharges are ignited at fairly high pressure as compared to H_2/CH_4 used for PCD deposition. As an example, for an input power of 600 W, optimal discharges are obtained at 200 mbar in $\text{Ar}/\text{CH}_4/\text{H}_2$ mixture and 25 mbar in CH_4/H_2 mixture. Also, the gas temperature was found to be much greater in $\text{Ar}/\text{CH}_4/\text{H}_2$ discharges as compared with H_2/CH_4 discharge for a given input power value. As a matter of fact, 2200 K gas temperature value was determined both numerically and experimentally for H_2/CH_4 plasmas obtained at 600 W and 25 mbar [8], while temperature values as high as 4000 K was measured in the bulk of $\text{Ar}/\text{H}_2\text{CH}_4$ discharges for the same input power level [9]. One of the main peculiarities of $\text{Ar}/\text{CH}_4/\text{H}_2$ discharges used for NCD deposition is probably the formation of soot particles that was often observed experimentally. Figure 2 shows a typical picture of the hemispherical $\text{Ar}/\text{CH}_4/\text{H}_2$ discharge with a cloud of emissive soot particles at the edge of the discharge. Such particles have never been observed in H_2/CH_4 plasmas used for PCD deposition.

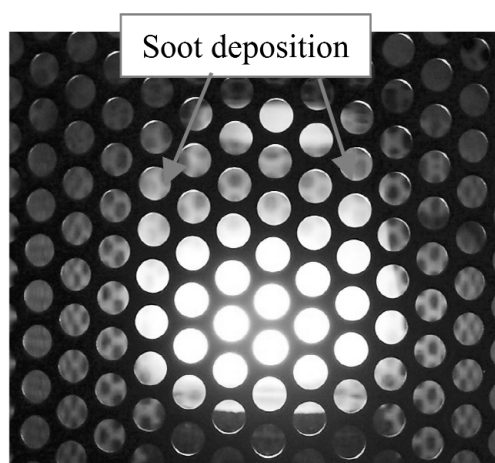


Fig. 2 A picture of a hemispherical optimal plasma obtained in the discharge system of Fig. 1. Reddish soot particles may be observed at the edge of the hemispherical discharge volume.

Although NCD may be deposited in a large range of pressure, the present work will focus on those discharges obtained at 200 mbar. Good-quality diamond films with grain size in the nanometer range were indeed obtained at this pressure [4]. The input power domain where optimal discharges may be obtained is intimately linked to the hydrogen content in the feed gas. The input power ranges necessary to ignite and sustain optimal hemispherical discharges at H_2 concentrations of 2 and 7 % are 300–500 W and 400–800 W, respectively [10]. The feed gas flow rate was set to 200 sccm, and the substrate temperature was around 900 °C.

THERMOCHEMICAL MODELS FOR $Ar/H_2/CH_4$ DISCHARGES

Qualitative analysis of the main physical and chemical characteristics of the investigated discharges

The plasmas considered in this work are characterized by a strong thermal and chemical nonequilibrium. The thermal nonequilibrium of the plasma is taken into account by distinguishing two energy modes: the heavy species translation–rotation (t–r) characterized by the gas temperature T_g and the electron translation (e). Due to the relatively high pressure, a thermal equilibrium was assumed between the vibrational modes of molecular species and the “t–r” mode of heavy species.

The formation of soot particles indicates that the chemistry in these discharges is fairly complex. The existence of large hydrocarbon (HC) molecules and ions is likely to take place and should be taken into account.

The temperature level achieved in the considered discharge is rather high. The temperature ranges between 600 K at the reactor wall and 4000 K in the plasma bulk. Large linear HC molecules and ions are not stable in this temperature range, and their formation is unlikely to be significant. In particular, attachment processes and formation of large linear HC negative ions are such as those observed in low-pressure radio frequency (RF) discharges, are unlikely to take place and will not be considered in this work [11,12]. On the contrary, the temperature domain encountered in the investigated reactor involves the temperature range at which large aromatic or polyaromatic HC molecules and ions may form significantly [13]. The growth of these large polyaromatic HC molecules and ions would, therefore, be the main route that can lead to the formation of soot particles through a homogeneous mechanism.

The chemistry models that we developed to describe the $Ar/CH_4/H_2$ sooty discharges used for the deposition of NCD rely on this assumption. It considers, therefore, that the chemistry involves two main groups of reactions. The first one describes the chemistry of small molecules usually obtained in plasma discharges where large molecule formation remains negligible. Basically, this first group of reactions includes $Ar/H/C$ species containing up to two carbon atoms. The second group of reactions considers the transition from small $C_{x<3}H_y$ species to HCs with a number of carbon atoms greater than two at temperature above 600 K. The main features of these two reaction groups are described in the next section.

Chemistry models for $Ar/H_2/CH_4$ plasmas

The chemistry of small molecules: The 2C model

The first submodel of $Ar/H_2/CH_4$ focuses on the discharge conditions where the formation of large HC molecules remains limited. This typically corresponds to high-temperature conditions encountered in the bulk of the plasma where HC species with more than two carbon atoms are at negligible concentration, as will be shown in the Results section. The 2C submodel corresponding to this condition is partly based on the model developed to describe H_2/CH_4 plasmas used for PCD deposition. It includes four reaction groups.

The first one describes the chemistry of hydrogen species: H_2 , H, $H(n = 2)$, $H(n = 3)$, H^+ , H_2^+ , and H_3^+ . It is derived from a detailed study performed on the chemistry in pure H_2 plasmas [14].

The second group of reactions describes the neutral chemistry of CH_{0-4} and C_2H_{0-6} species. Several groups working on either combustion or HC pyrolysis extensively investigated this chemistry. We used the reaction model recommended in the GRI-Mech mechanism database [15].

The third group of reaction deals with HC ion kinetics. It corresponds, with slight improvements, to the reaction scheme developed to describe ion kinetics in H_2/CH_4 discharges used for PCD deposition. The ionic species considered are C^+ , CH_3^+ , CH_4^+ , CH_5^+ , C_2H_6^+ , C_2H_5^+ , C_2H_4^+ , C_2H_3^+ , C_2H_2^+ , C_2H^+ , and C_2^+ . The reactions involve electron-impact ionization, dissociation and dissociative ionization processes for HCs, ion conversion processes involving H_3^+ and several C_xH_y^+ ions, and dissociative recombination for HC ions. The collisional data used for these reactions are discussed in [16,17].

The last group of reactions in this first submodel deals with processes involving argon-containing species. These are Ar , Ar^* , Ar^+ , ArH^+ , and ArH^{+*} . Ar^* represents the four metastable-resonant states of argon with energy around 11 eV that should be in collisional equilibrium at the high pressure considered here. The details on the reaction experienced by argon-containing compounds may be found in [9].

Formation and growth of large molecular and ionic HCs: The A4/A9 and A4⁺ models

Besides the 2C submodel used to describe the chemistry of species with less than two carbon atoms in $\text{Ar}/\text{H}_2/\text{CH}_4$ discharges, we used three additional models that describe the formation of aromatic HCs and their molecular growth. The first two models, the A4 and A9 submodels, describe the growth of neutral HCs while the third one, the A4⁺ submodel, describes the formation and growth of positively charged ionic HCs.

Neutral polycyclic aromatic hydrocarbon (PAH) kinetics and the A4/A9 models

The formation of neutral HC was described using the hydrogen abstraction carbon addition (HACA) model (i.e., HC abstraction/carbon addition) proposed by Frenklach et al. [18]. In this model, the small HC precursor for aromatic compounds is assumed to be acetylene. The transition from small species (i.e., less than two carbon atoms) to aromatic compounds starts with a linearization process that leads to the formation of the C_4H_3 and C_3H_3 radicals.

These radicals undergo cyclization reactions that result in the production of the phenyl radical [18]. Once this phenyl radical is obtained, the growth of aromatic HC molecule proceeds by the HACA mechanism proposed by Frenklach [18] and depicted below.

The mechanism schematized in Fig. 3 may be initiated with any large PAH molecules and results in a molecular growth through the addition of one aromatic increase at each step.

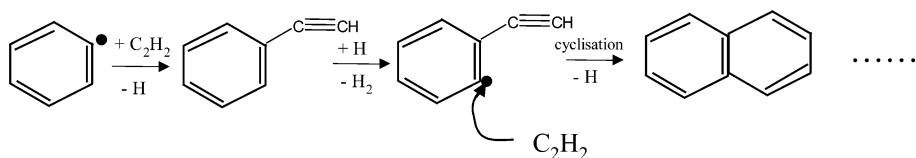


Fig. 3 Schematic of the HACA mechanism.

Note also that beside the processes schematized in Fig. 3, there are several other processes that lead to the formation of branched PAH. The details of all these process involved in the molecular growth of PAH may be found in refs. [13,18,19].

Two molecular growth processes were considered in this work. In the first one, denoted the A4 model, we track the molecular growth up to the pyrene, a four-ring PAH, and we consider that the nucleation results from the condensation of two pyrene molecules. In this case, the largest molecular edifice is the pyrene molecule. In the second model, denoted the A9 model, we follow the growth of the HC molecules up to a nine-ring PAH, the dibenzocoronene, and we consider that the nucleation process results from the condensation of the dibenzocoronene species. In this A9 model, the largest molecular

edifice is considered to be the dibenzocoronene species. The main purpose in considering this A9 model was to investigate how the choice of the size of the largest molecular edifice affects the nucleation kinetics predicted by the model.

To summarize, the A4 model includes the 2C model described in the last section and the chemistry of large PAH molecule up to four-ring species. This results in a 101 species/356 reaction kinetic scheme. The A9 includes the 2C model described in the last section and the chemistry of large PAH molecule up to four-ring species. This results in a 202 species/765 reaction kinetics scheme. It is worth mentioning that the interaction between the electrons and the large PAH molecules is not considered in the A4 and A9 models.

Charged PAH kinetics and the A4⁺ submodel

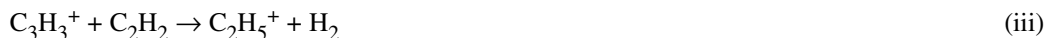
To our best knowledge, there is only one molecular growth model through positive ions. This was proposed by Calcote et al. [20,21] to explain the formation of soot in flames.

This mechanism assumes that the main precursor ion for the development of large ions is C₃H₃⁺. For the discharge conditions considered in this work, there are only two reactions that may lead to the formation of this ion. These are:



The rate constant of the last process was taken from Brown and Eraslan [22].

Once C₃H₃⁺ is formed, it induces two linearization processes, where acetylene plays a key role, that will initiate two ion growth routes for the even and odd ions, respectively. These processes are:



Addition of a further acetylene molecule on C₅H₃⁺ and C₄H₃⁺ leads to the formation of 6- and 7-carbon linear ions that undergo spontaneous cyclization processes through a further addition to acetylene. The obtained aromatic ions are depicted in Fig. 4.

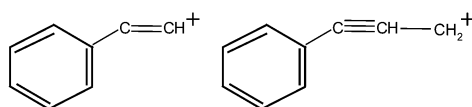


Fig. 4 Chemical structure of the smallest aromatic ions predicted by Calcote mechanism (A4⁺ models).

Once these ions are formed, the ion growth process takes place through the addition of acetylene molecules and elimination of hydrogen molecule [20,21].

The ions with a number of carbon x , such as $x = 4k$ or $x = 4k + 1$, undergo cyclization. Most of the ionic species are, therefore, substituted polyaromatic HC.

The growth of HC ions was tracked up to four-ring HCs (17 carbon atoms), and we assume that a further growth above this size spontaneously leads to a nucleation process.

The inclusion of electron-large HC interaction in the A4⁺ model requires describing the electron-impact ionization of HC species with more than three carbons. This task is very difficult since almost nothing is known about the kinetics of these ions in plasma phase. There is no data for the electron-impact ionization and dissociation of aliphatic molecules with more than two carbon atoms (except propane). As for the aromatic species ionization, cross-section data are only known for benzene. Describing the details of the large HC ions kinetics is, therefore, impossible and is not the objective of the present work. Our main purpose here is to determine if the ionic mechanism proposed by Calcote

[20,21] can compete with the HACA mechanism proposed by Frenklach [13,18] in the growth kinetics of HC under discharge conditions. To reach this goal, we built up a small qualitative model where we consider that PAH ions interact with electrons through the following processes:

- Electron-impact ionization:



- Three-body recombination:



- Dissociative recombination:



The rate constants of the three-body recombination processes rn. vi are given by Brown et al. [22], while Calcote [20,21] gives an expression to evaluate the equilibrium ionization constant $K_{\text{vi/vii}}$ (chemical equilibrium corresponding to process rns. v and vi. The electron-impact ionization rate was estimated from the equilibrium constant $K_{\text{vi/vii}}$ and the rate constant k_{R13} . The rates for dissociative recombination are known for some large aromatic ions [23–25]. These are in the range 10^{-7} – 10^{-6} $\text{cm}^3 \text{s}^{-1}$. We therefore used a value of 10^{-6} for all the dissociative recombination process rn. vii. The rate constants of ion addition processes were estimated using the Langevin theory as described by Gioumousis et al. [26], Brown et al. [22], Calcote et al. [20,21], and Eraslan et al. [27].

The A4⁺ reaction model includes the reaction of the 2C model, the A4 model, and the HC ion kinetics described in this section. This results in a 121 species/401 reaction kinetics model.

Estimation of the plasma composition and temperatures in the frame of the quasi-homogenous plasma model

The four thermochemical models, 2C, A4, A9, and A4⁺, discussed above are used to describe the investigated discharge in the frame of a quasi-homogenous plasma model. The details of this model are described in [14], and we will only summarize its main feature here. We assume that the discharge is made of a homogenous plasma volume where all the plasma characteristics are constant and of a thin boundary layer through which species and energy transfer from the bulk of the plasma to the substrate surface take place. Species densities and plasma temperatures are assumed to vary linearly in this boundary layer (Fig. 5). Under this assumption, the time evolutions of species densities in the bulk of the discharge are governed by a set of ordinary differential equations that may be written as [14,28]

$$\frac{dy_i}{dt} = \frac{w_i + R_i}{\rho} \quad (1)$$

where y_i is the mass fraction of species “ i ”, and ρ is the total plasma density. w_i and R_i are the net production rates of species “ i ” by gas-phase processes and surface processes, respectively. The method used to estimate w_i and R_i is discussed in details in ref. [14].

The net production rate w_i depends on the species density and the reaction rate constants of the chemical processes involved in the kinetics model. As far as rate constant estimation is concerned, two cases may be distinguished: (i) heavy species–heavy species collision rate constants and (ii) electron-heavy species collision rate constants.

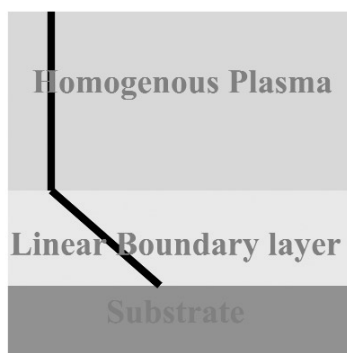


Fig. 5 Schematic principle of a quasi-homogeneous plasma model.

In principle, electron-heavy species rate constants depend on the electron energy distribution function that deviates from a Maxwellian distribution for the considered discharges. This means that the solution of the species balance (eq. 1) would, in principle, require coupling the electron Boltzmann equation. However, previous studies have shown that for moderate pressure discharges, the electron-heavy species reaction rate constants only depend on the electron-average energy and that the knowledge of the whole electron energy distribution function is not necessary to estimate these rate constants. This brings an important simplification to our model, since instead of coupling the electron Boltzmann equation to the species equations we just need to consider an electron-average energy equation. The dependence between the rate constant and the electron-average energy can be determined independently by using an off-line Boltzmann solver.

The electron-average energy considered in this model may be written as [14]

$$\frac{d \langle \varepsilon_e \rangle}{dt} = \frac{\text{MWPD}_{\text{av}} - Q_{e-t} - Q_{e-v} - Q_{e-\chi} - J_{e-\text{sub}} h_e \frac{S_{\text{sub}}}{V_{\text{plasma}}}}{\rho_e} \quad (2)$$

$\langle \varepsilon_e \rangle$ is the electron-average energy. MWPD_{av} is the average microwave power density absorbed by the electrons and is given by the ratio of the absorbed power to the plasma volume. Q_{e-t} , Q_{e-v} , and $Q_{e-\chi}$ are the rates of the energy dissipated by electron during energy transfer to the translational mode of heavy species, energy transfer to the vibrational mode of molecular species, and during the activation of chemical processes. The rate of energy transfer between the translational modes of electron and heavy species is estimated from the elastic collision cross-sections and the difference between the electron and heavy species temperature as described in [29]. The rate of energy transfer between the electron and the vibrational modes is estimated from the electron-impact vibrational excitation rate constants and the population of the vibrational levels as estimated using the assumption of a thermal equilibrium between the vibrational and the translational modes of heavy species [29]. Similarly, the rate of energy dissipation through electron-impact chemical processes is estimated from the rate constants of the chemical processes and their activation energy as described in [29]. $J_{e-\text{sub}}$, h_e , and ρ_e are the electron flux at the substrate, the electron enthalpy, and the electron mass density. S_{sub} and V_{plasma} are the substrate area and the plasma volume.

The heavy species–heavy species reaction rate constants depend on the gas temperature. This is determined by coupling to species and electron energy equations a total energy equation that may be written as [14]

$$\frac{dE}{dt} = \frac{\text{MYPD}_{av} - Q_{\text{rad}} - \left[\sum_i J_{i-\text{sub}} h_i + \lambda \frac{T_g - T_{\text{sub}}}{\delta} \right] \frac{S_{\text{sub}}}{V_{\text{plasma}}}}{\rho} \quad (3)$$

E is the total average energy, Q_{rad} is the rate of energy loss by radiation, λ is the thermal conductivity, and T_{sub} is the substrate temperature. δ is the thermal boundary layer thickness. $J_{i-\text{sub}}$ and h_i are the flux at the substrate and the enthalpy of species “ i ”. ρ is the total mass density.

The surface net production rates R_i depend on the substrate temperature, the boundary layer thickness, and the recombination/de-excitation coefficients and the diffusion coefficients of the different species. The way these rates are estimated is extensively discussed in [14], which also gives the values adopted for the recombination/de-excitation coefficients. The transport coefficients, diffusion and conductivity, were estimated from the reduced collision integrals based on Lennard–Jones interaction potential [30,31].

For a given discharge condition (i.e., microwave power density and pressure and feed gas composition), the steady-state plasma composition is calculated by time-integrating the coupled set of species and energy balance eqs. 1–3. The integration starts from a plasma composition corresponding to a cold gas with a very small electron density (this is necessary to initiate the ionization process). The microwave power density leads to electron heating, strong ionization and dissociation kinetics, gas heating, and enhanced thermal chemistry. The resulting change in the gas composition and electron and gas temperature is calculated by time-integrating the balance eqs. 1–3. The numerical algorithm makes use of fully implicit backward difference formulae (BDF) of Gear [32]. The integration is stopped once the species densities and the electron and gas temperature reach the steady state.

RESULTS AND DISCUSSION

All the simulation discussed in this section corresponds to a discharge pressure of 200 mbar.

The first discharge simulations were performed using the 2C model without taking into account the possible production of large HC species. We remind here that when the input microwave power is increased from 500 to 800 W, the H_2 amount in the feed gas is varied from 2 to 7%, which enables us to keep optimal discharge conditions for NCD deposition. Figure 6 shows the evolution of the bulk gas temperature as a function of the input microwave power. In the same figure, we also report the rotational temperatures of $\text{C}_2(a^3\Pi_u)$ and $\text{C}_2(d^3\Pi_g)$ measured by absorption and emission spectroscopy. It is worth mentioning that when using this technique, the temperature is estimated from line-of-sight measurements and corresponds therefore to an average over the entire region, where C_2 molecule is present at a sufficiently high concentration. Consequently, only qualitative comparison between calculated and measured temperatures can be performed. The calculated gas temperature ranges between 4000 and 4200 K when the input power increases from 500 to 800 W. The measured rotational temperatures are slightly lower than the calculated ones. They also show quite small variations and remain around 3200 K in the investigated power range. Note that the slight decrease in the measured rotational temperature in the power domain ranging between 700 and 800 W may be due a small increase in the actual plasma volume and a subsequent decrease in the power density that actually controls the temperature in the bulk of the plasma. Since the discharge is very emissive, such a change in the plasma volume is very difficult to observe. Taking into account the peculiarity of the absorption measurements techniques (line of sight) and the different assumption made in the frame of the quasi-homogeneous plasma model, the experimental and calculated temperatures can be considered in a qualitative good agreement. They both show that the temperature of the considered discharge are high in the range 3200–4200 K and does not significantly vary with the input power.

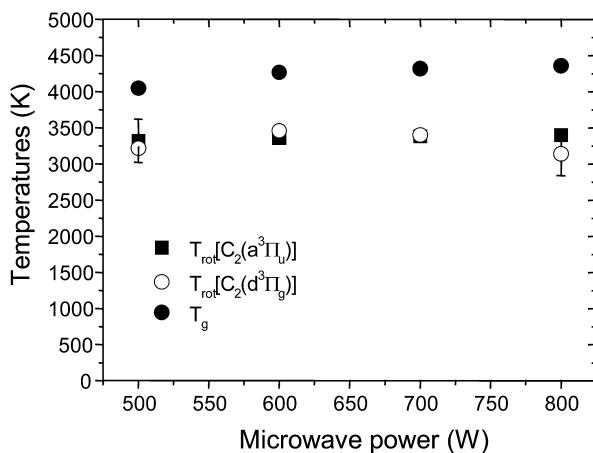


Fig. 6 Variation of the calculated gas temperature (T_g) and of the rotational temperatures of $C_2(a^3\Pi_u)$ and $C_2(d^3\Pi_g)$ with the input microwave power.

Figure 7 shows the variation of H-atom mole fraction as function of the input microwave power density for two values of the H_2 concentration in the feed gas. The H-atom mole fraction is very high and much higher than would be obtained from the total dissociation of H_2 that is almost totally dissociated under the investigated discharge conditions. As an example, the H-atom mole fraction at 500 W and 2 % H_2 in the feed gas is 0.075, which exceeds by far the value that should be obtained (i.e., 0.04) if H-atom would have been only produced by H_2 dissociation. This means that a large fraction of H-atom comes from the dissociation of CH_4 . The latter is also totally converted into HC molecules with smaller H/C ratio.

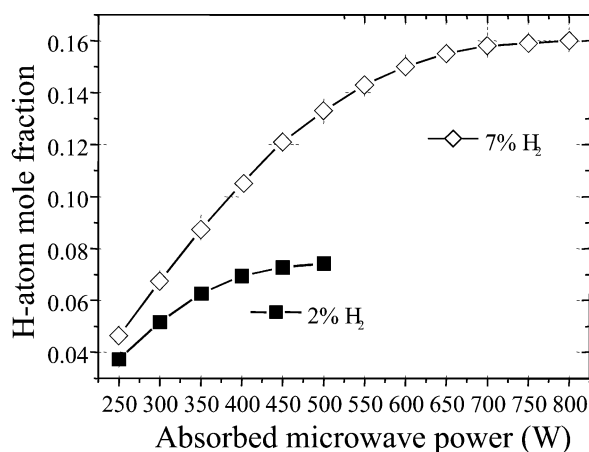


Fig. 7 Variation of the calculated H-atom mole fraction with the input microwave power for 2 % H_2 in the feed gas: 2 and 7 %.

Figures 8a, 8b, and 8c show the variation of the major neutral carbon-containing species with the input microwave power. Three main power domains may be distinguished. The first one corresponds to low input power values where acetylene is the major carbon-containing species. Then, when power increases, acetylene density strongly decreases while C_2 and C become the dominant carbon species. If the power is further increased, the only dominant carbon species is C. The power values at which tran-

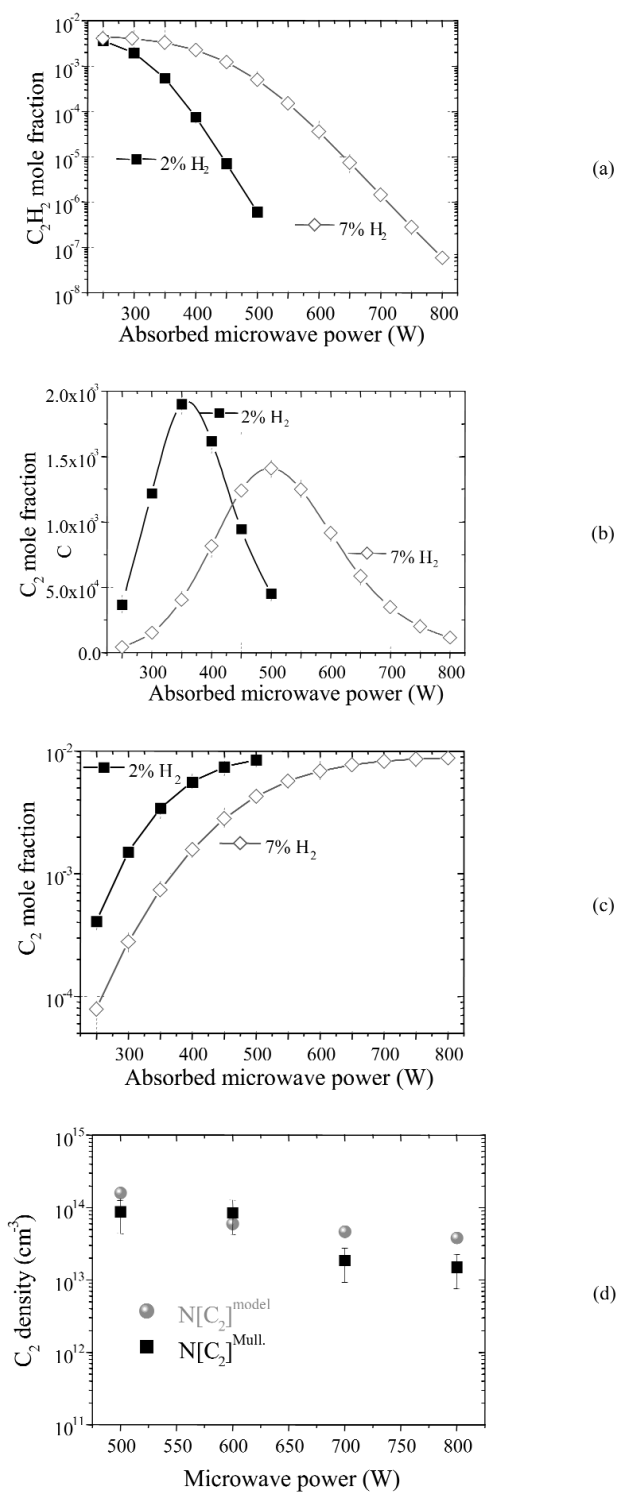


Fig. 8 Variation of C_2H_2 (a), C_2 (b), and C (c) densities with the input microwave power for two values of the hydrogen concentration in the feed gas. (d) Comparison of the calculated C_2 densities with those measured by absorption spectroscopy performed on the Mulliken system.

sitions from acetylene to C_2 , and then to C take place depends on the amount of H_2 in the feed gas. The acetylene predominance domain corresponds to input power below 300 W for 2 % H_2 in the feed gas and extends up to an input power of 500 W for 7 % H_2 in the feed gas. The $C_2H_2 \rightarrow C_2 \rightarrow C$ transition process induces a pronounced maximum concentration in the variation of C_2 with the input power. Figure 8d shows a comparison between the C_2 densities predicted by the model and measured by absorption on the Mulliken system for optimal discharge configurations. Fairly good qualitative agreement is obtained between the model and the experiment, which gives similar order of magnitudes and trends in the variation of C_2 density with the input power. Both measurement and calculations show indeed that the C_2 density is in the range 10^{13} – 10^{14} cm^{-3} and significantly decreases when increasing the input power.

These first results show that the 2C model enables us to accurately predict some features of the discharge bulk such as the gas temperature and the C_2 density. We may, therefore, use this 2C model as a starting point to analyze the soot formation with the help of the A4, A9, and A4⁺ models. The soot nucleation will, however, be investigated as a function of the gas temperature that was varied between 1200 and 4000 K by varying the input power from 10 to 800 W (see Fig. 9). Of course, 10-W input power does not correspond to a real discharge situation, it is just a simple and convenient way to simulate relatively low temperature conditions. Temperature values around 1200 K will be representative of the chemistry at the discharge edges and near the substrate surface, while temperature as high as 4000 K will be characteristic of the plasma bulk. Figure 9 shows the simulated input power conditions that yield the whole temperature range in the reactor.

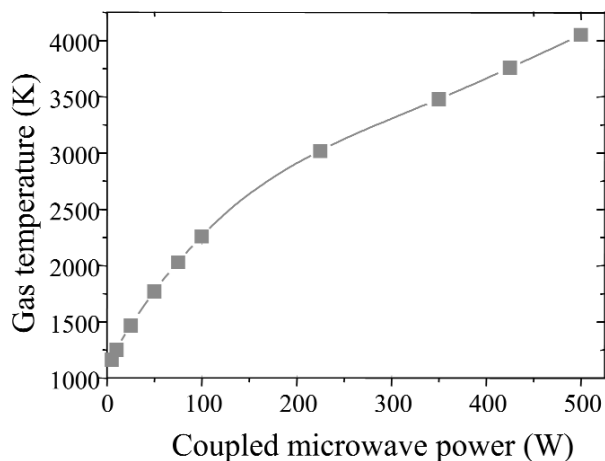


Fig. 9 Gas temperature range obtained by a simulated variation of the input power.

Figure 10 shows a comparison between the densities predicted for the major small carbon-containing species by the 2C and the A4 models at high (500 W–4050 K) and low (25 W–1470 K) temperature. The 2C and A4 models give almost exactly the same results at high temperature (Fig. 10a). The two models predict the predominance of C, C_2 , C_2H , and C_2H_2 over all the other species at high temperature. They also predict a significant ionization of C_2 and C that show, however, densities below those of ArH^{*+} , which represents the major positive ion.

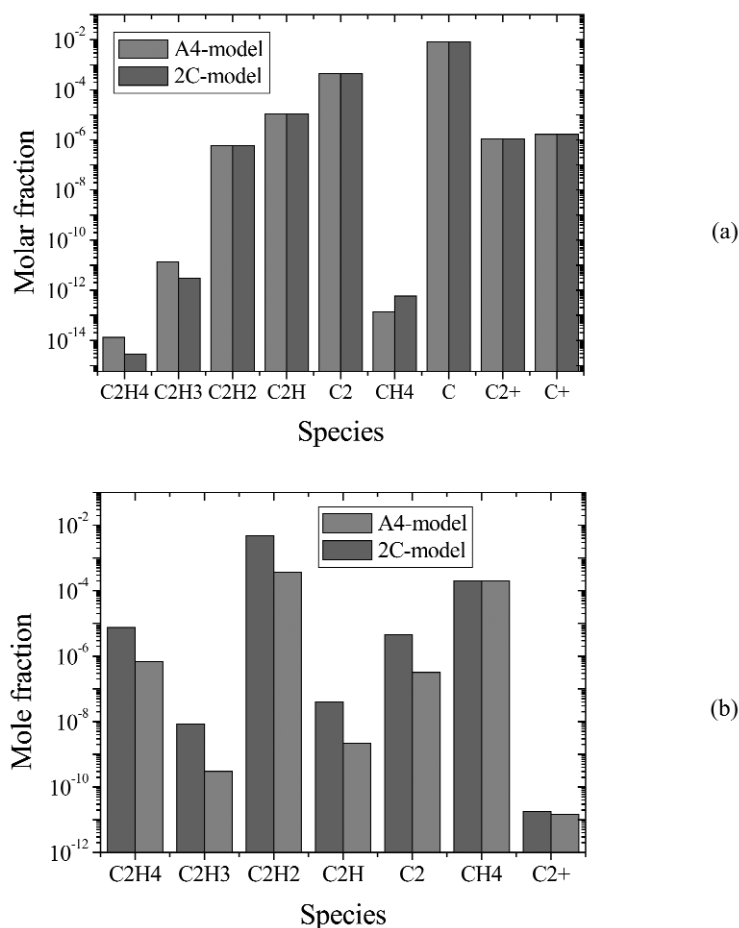


Fig. 10 Mole fractions of the major species with fewer than three carbon atoms at 500 W/4050 K (a) and 25 W/1470 K (b).

The situation is significantly different at low temperature (Fig. 10b). In this case, the 2C and A4 models give very different predictions. The density values predicted by the two models for acetylene that represent the predominant two-carbon-containing species differ by one order of magnitude. The same difference is obtained for other small molecules such as C₂H₄ and C₂. The A4 model predicts that the small molecules with a number of carbons less than two do not carry the major part of the carbon introduced in the reactor. A large fraction of the carbon is indeed stored in the form of aromatic molecules. This is shown in Fig. 11, where we report the variation of the major aromatic species as a function of the gas temperature. This figure shows that aromatic molecules such as benzene (A1), naphthalene (A2), and acenaphthylene (A2R5) are present at significant concentrations. The PAH molecules taken into account in the A4 model store more than 50 % of the carbon introduced in the discharge.

Figure 11 also shows that the PAH mole fraction strongly decreases when the temperature becomes greater than 1500 K. Above this temperature value, the HC kinetics is dominated by the C₂H₂ → C₂ → C conversion. Below this temperature, the dominant processes are the linearization/cyclization mechanisms leading to the formation and the development of PAH molecules. This result indicates that the radical A4 mechanism would lead to PAH molecule growth and soot particles production in the relatively *cold* region of the reactor at the discharge edge and in the vicinity of the substrate.

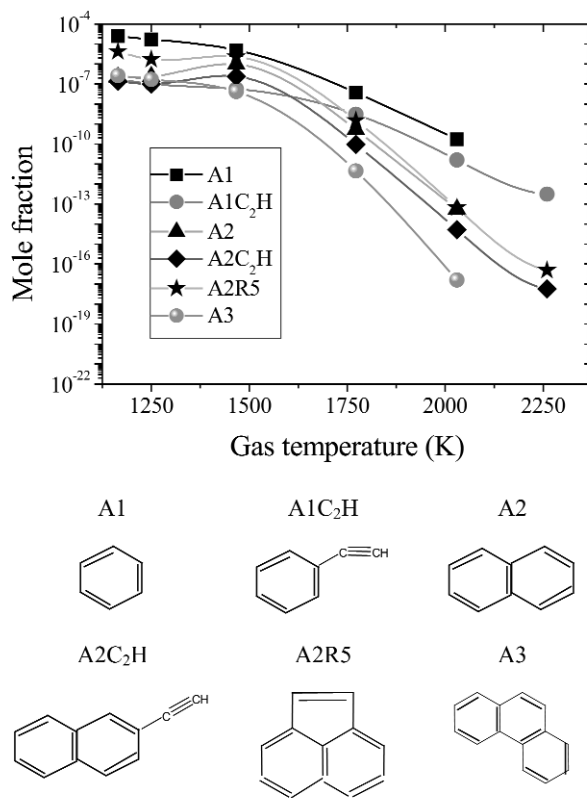


Fig. 11 Variation of the densities of the major PAH as function of the temperature. The chemical structures of these major species are also given.

Figure 12a shows the dynamic of soot nucleation through the A4 mechanism at different values of the gas temperature for discharge duration of 10 000 s that corresponds to the duration of the NCD deposition process. At low temperature, the nucleation starts after a few seconds, its rate reaches a maximum after discharge duration of 10–20 s and then decreases. The nucleation rate reaches a maximum around 10^{13} nuclei $\text{cm}^{-3} \text{s}^{-1}$ for temperatures of 1170 and 1250 K. The maximum nucleation rate decreases to 3×10^{12} nuclei $\text{cm}^{-3} \text{s}^{-1}$ for a temperature of 1470 K. For much higher temperature, 1750 K, the nucleation starts very early during the discharge phase (less than 1 s). The maximum nucleation rate remains, however, quite small with a value around 8×10^9 nuclei $\text{cm}^{-3} \text{s}^{-1}$. The nucleation decreases to 10^7 nuclei $\text{cm}^{-3} \text{s}^{-1}$ after only 10 s discharge duration. Figure 12b shows the time average nucleation rate during all the discharge duration, i.e., 10^4 s. The soot production rate is almost constant for gas temperature between 1100 and 1500 K and strongly decreases for temperature values above 1500 K. This shows once again that the A4 mechanism would lead to a significant soot nucleation only in the vicinity of the substrate surface and near the discharge edges. No soot nucleation would be obtained in the plasma bulk.

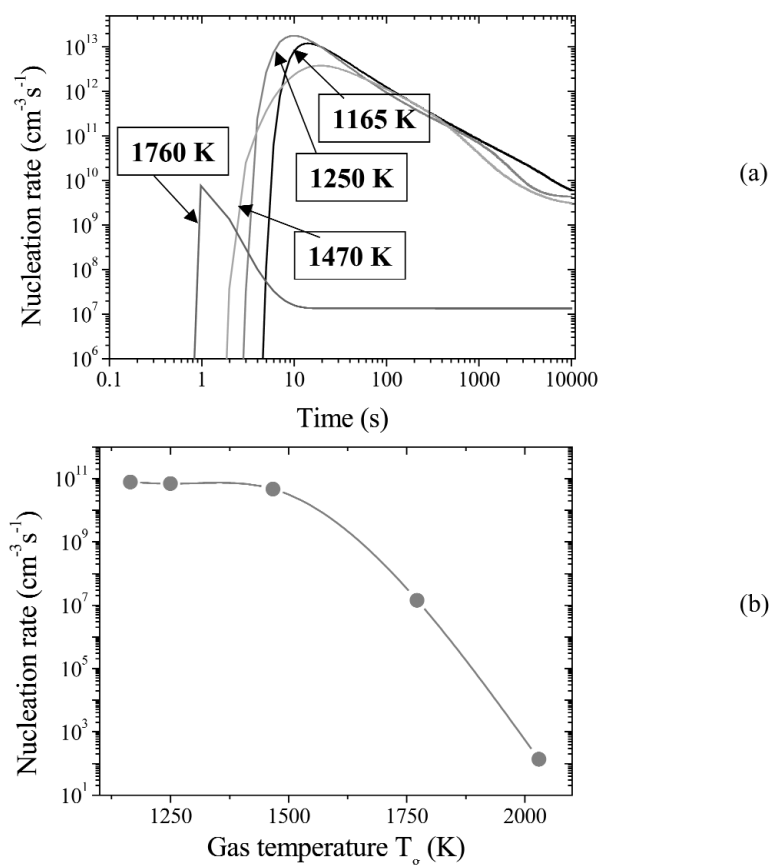


Fig. 12 (a) Time variation of the soot nucleation rate at different gas temperatures. (b) Time-averaged nucleation rate over the duration of the deposition process (10^4 s).

To investigate how the assumption made on the molecule size at which nucleation takes place affects the predicted nucleation dynamics and the overall soot production rate, we performed simulations with two models. The A4 model where the molecular growth is tracked up to four-ring species and the nucleation is assumed to take place by condensation of two pyrene molecules and the A9 model where the molecular growth is tracked up to nine-ring PAH species and the nucleation is assumed to take place by the condensation of two dibenzocoronene molecules. Results are shown in Fig. 13. Basically, the nucleation dynamics obtained with the A4 and the A9 models show the same trends. The maximum values of the nucleation rate obtained by the two models have almost the same order of magnitude for the two considered temperature values. The two models also predict similar values for the time at which these maxima are reached (Fig. 13a). The variations of the average nucleation rates over all the deposition time (10^4 s) obtained from the two models with the gas temperature are shown in Fig. 13b. The two models give the same trends again, although the A9 model predicts smaller nucleation rate and wider nucleation temperature domain.

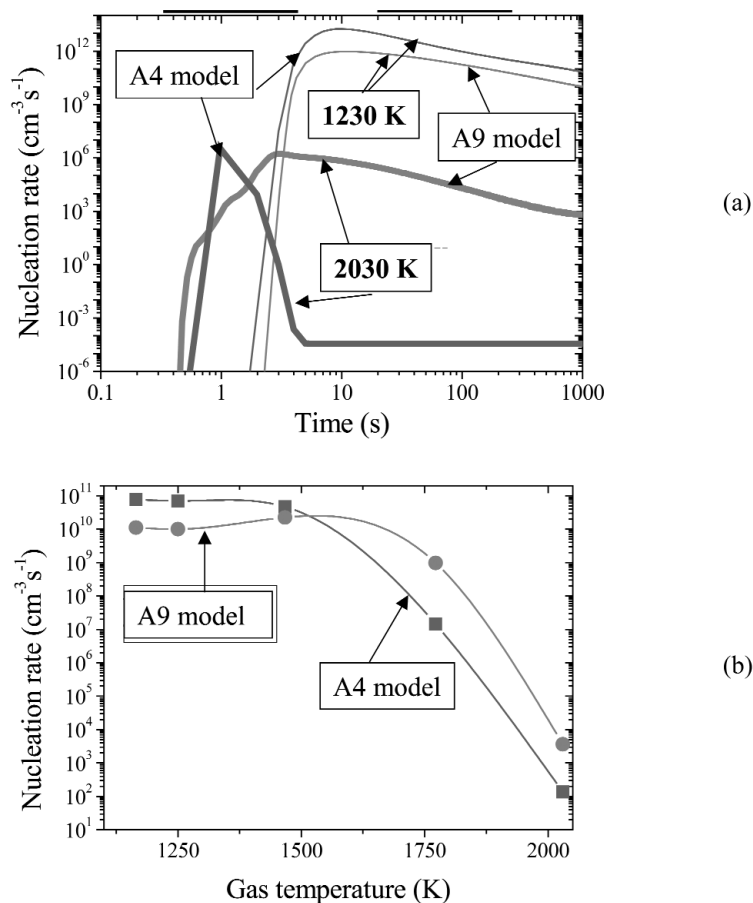


Fig. 13 (a) Time variation of the soot nucleation rate obtained from the A4 and A9 models. (b) Time-averaged nucleation rate over the duration of the deposition process (10^4 s) obtained from the A4 and A9 models.

The similarity between the A9 and A4 models is not surprising since the molecular growth kinetics is controlled to a large extent by the linearization/cyclization, processes. These are treated in the same way in the two models. The slightly slower nucleation dynamics (Fig. 13a) and smaller nucleation average rates (Fig. 13b) predicted by the A9 model, may be explained by the requirement in the case of this model to track the molecular growth over a much greater number of species. Roughly speaking, the nucleation kinetics in the A9 model would correspond to the nucleation kinetics in A4 model with a time lag due to the molecular growth from four- to nine-ring molecules.

The last sets of simulations were performed with the A4⁺ model in order to investigate the efficiency of this ionic mechanism to produce soot particles. Results obtained with this model also showed that PAH show significant concentration only for gas temperature below 1500 K. The ratio of HC neutral and their corresponding ion were found to be less than 10^{-2} for almost all the discharge conditions investigated here. This is shown in Fig. 14a where the ratio of charged to neutral PAH is shown for three gas temperature conditions corresponding to three reactor regions: the bulk plasma, an intermediate position, and outside the discharge.

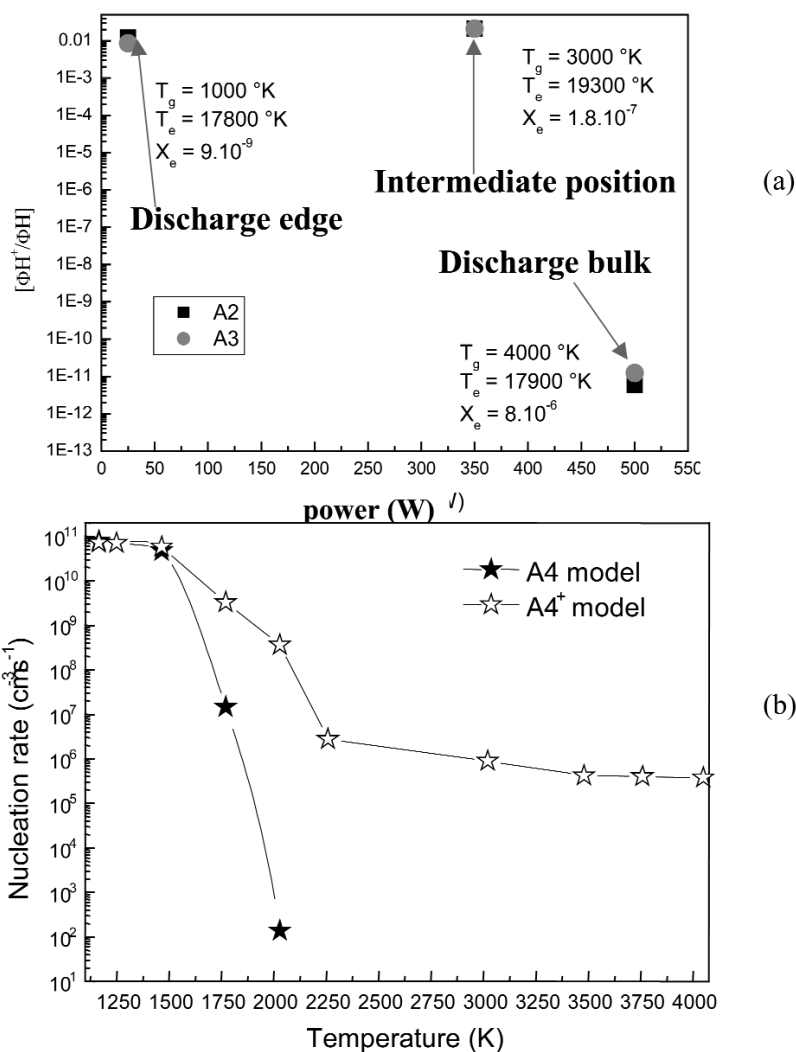


Fig. 14 (a) Ratio of the ion to neutral density at different discharge conditions. (b) Time-averaged nucleation rate over the duration of the deposition process (10^4 s) obtained from the A4 and A4⁺ models.

Figure 14b shows the variation of the time-averaged nucleation rates over all the deposition process duration (10^4 s) predicted by the A4 and A4⁺ models. At low gas temperature, when the nucleation is significant, the two models yield almost the same nucleation rates. However, when the temperature increases, the A4⁺ model predicts much higher nucleation rate than the A4 model. Note, however, that this difference is not of a major importance since in this condition the nucleation rate predicted by the two models are not significant.

This result shows that the production of soot by the ionic mechanism proposed by Calcote is by far less significant than by the HACA mechanism of Frenklach for conditions where soot nucleation is significant. The ionic mechanisms turn out to be much more efficient than the radicalar mechanism only at high temperature where soot nucleation may be disregarded.

CONCLUSION

The modeling work presented in this paper showed that the HACA mechanism proposed by Frenklach could explain soot formation in Ar/H₂/CH₄ discharges. More specifically, this formation was predicted to be optimal at relatively low temperature (i.e., 1000–1500 K), which is consistent with the experimental observation that shows that soot tends to form in the region outside the discharge (see Fig. 2). The ionic growth route proposed by Calcote seems to be much less significant in producing soot under our discharge conditions. The existence of other ionic routes may be however possible. The assessment of other possible ionic mechanisms requires, however, the development of some experimental investigation on the large molecules and ions formed in the plasma. The soot formation models presented in this work make use of quite simple description, of the nucleation process, i.e., the concept of “largest molecular edifice”. The implication of the assumption made on the largest molecular edifice was analyzed by comparing two models that considers largest molecular edifices with different sizes. Results showed that the two models yield at least qualitatively quite similar results. Taking into account the large neutral HCs turns out to be necessary for an accurate description of the cold region of the reactor, while models that only take into account small molecules may accurately describe the bulk of the discharge. In particular, the C₂ model presented in this paper enables us to accurately predict the gas temperature and the density of C₂ species.

This work represents a first step in the investigation of these Ar/H₂/CH₄ sooty discharges. The understanding of these discharges requires answering several questions. First of all, the molecular growth models presented in this paper should be coupled to aerosol dynamic models to study how the particles can affect the plasma chemistry through heterogeneous process. Also, transport phenomena should be taken into account in the analysis of the discharge. At least a 1D transport model that includes the thermochemical models discussed in this paper should be indeed developed to analyze if these particles that form at the edge of the discharge can be transported into the plasma bulk and involved in a heterogeneous chemistry that affects the discharge characteristics.

REFERENCES

1. J. C. Angus, C. C. Hayman. *Science* **214**, 913 (1988).
2. D. M. Gruen, X. Pan, A. R. Krauss, S. Liu, J. Luo, C. M. Foster. *J. Vac. Sci. Technol. A* **12**, 1491 (1994).
3. F. Bénédict, M. B. Assouar, F. Mohasseb, O. Elmazria, P. Alnot, A. Gicquel. *Diamond Relat. Mater.* **13**, 347 (2004).
4. P. Bruno, F. Bénédict, F. Mohasseb, G. Lombardi, F. Silva, K. Hassouni. *J. Phys. D: Appl. Phys.* **37**, L35 (2004).
5. A. Gicquel, E. Anger, M. F. Ravet, D. Fabre, G. Scatena, Z. Z. Wang. *Diamond Relat. Mater.* **2**, 417 (1993).
6. C. Findeling-Dufour, A. Vignes, A. Gicquel. *Diamond Relat. Mater.* **4**, 429 (1995).
7. M. T. Swihart, S. Nijhawan, M. R. Mahajan, S.-M. Suh, S. L. Girshick. *J. Aerosol Sci.* **29**, 79 (1998).
8. A. Gicquel, M. Chenevier, Y. Breton, M. Petiau, J. P. Booth, K. Hassouni. *J. Phys. III* **6**, 1167 (1996).
9. G. Lombardi, K. Hassouni, F. Bénédict, F. Mohasseb, J. Röpcke, A. Gicquel. *J. Appl. Phys.* **96**, 6739 (2004).
10. F. Bénédict, F. Mohasseb, P. Bruno, G. Lombardi, K. Hassouni, A. Gicquel. In *Synthesis, Properties and Applications of Ultrananocrystalline Diamond*, D. M. Gruen, O. Shenderova, A. Ya. Vul' (Eds.), pp. 79–92, NATO Science Series, Mathematics, Physics and Chemistry – Vol. 192, Springer (Kluwer Academic) (2005).
11. S. Stoykov, C. Eggs, U. Kortshagen. *J. Phys. D: Appl. Phys.* **34**, 2160 (2001).

12. S. Hong, J. Berndt, J. Winter. *Plasma Sources Sci. Technol.* **12**, 46 (2003).
13. M. Frenklach, T. Yuan, M. K. Ramachandra. *Energy Fuels* **2**, 462 (1988).
14. K. Hassouni, A. Gicquel, M. Capitelli, J. Loureiro. *Plasma Sources Sci. Technol.* **8**, 494 (1998).
15. G. P. Smith, D. M. Golden, M. Frenklach, R. W. Moriarty, B. Eiteneer, M. Goldenburg, C. T. Bowman, R. K. Hanson, S. Song, W. C. J. Gardiner, V. V. Lissiansky, Z. Qin. *Gri-Mech 3.0*: <http://www.me.berkeley.edu/gri_mech/>.
16. H. Tawara, Y. Itakawa, H. Nishimura, H. Tanaka, Y. Nakamura. *NIFS-DATA Research Report* **6** (1990).
17. H. Tahara, K. I. Minami, A. Murai, T. Yasui, T. Yoshikawa. *Jpn. J. Appl. Phys.* **34**, 1972 (1995).
18. H. Wang, M. Frenklach. *Combust. Flame* **110**, 173 (1997).
19. H. Wang, M. Frenklach. *J. Phys. Chem.* **97**, 3867 (1993).
20. H. F. Calcote. *Combust. Flame* **42**, 215 (1981).
21. H. F. Calcote, D. G. Keil. *Combust. Flame* **74**, 131 (1988).
22. R. C. Brown, A. N. Eraslan. *Combust. Flame* **73**, 1 (1988).
23. J. B. A. Mitchell, C. Rebrion-Rowe, J. L. Le-Garrec, G. Angelova, H. Blume, K. Seiersen. *Int. J. Mass Spectrom.* **227**, 273 (2003).
24. G. Angelova, O. Novotny, J. B. A. Mitchell, C. Rebrion-Rowe, J. L. Le-Garrec, H. Bluhme, K. Seiersen, L. H. Andersen. *Int. J. Mass Spectrom.* **232**, 195 (2004).
25. G. Angelova, O. Novotny, J. B. A. Mitchell, C. Rebrion-Rowe, J. L. Le-Garrec, H. Bluhme, K. Seiersen, L. H. Andersen. *Int. J. Mass Spectrom.* **235**, 7 (2004).
26. G. W. Gioumoussis, D. P. Stevenson. *J. Chem. Phys.* **29**, 294 (1958).
27. A. N. Eraslan, R. C. Brown. *Combust. Flame* **74**, 19 (1988).
28. K. Hassouni, X. Duten, A. Rousseau, A. Gicquel. *Plasma Sources Sci. Technol.* **10**, 61 (2001).
29. K. Hassouni, C. D. Scott, S. Farhat, A. Gicquel. In *Industrial Handbook for Diamond and Diamond Films*, M. Prelas, K. Bigelow, G. Popovicci (Eds.), pp. 653–672, Marcel Dekker, New York (1997).
30. R. B. Bird, W. E. Stewart, E. N. Lightfoot. *Transport Phenomena*, John Wiley, New York (1960).
31. R. J. Kee, F. M. Rupley, J. A. Miller. *CHEMKIN-III: A FORTRAN chemical kinetics package for the analysis of multi-fluid gas-phase chemical kinetics*, Sandia National Laboratories Report (1996).
32. K. Radhakrishnan, A. C. Hindmarsh. *NASA, UCRL-ID-113855* (1993).